Journal of Computational Physics **168,** 1–25 (2001)
doi:10.1006/jcph.2000.6670, available online at http://www.idealibrary.com on IDEAL®

The Surface Gradient Method for the Treatment of Source Terms in the Shallow-Water Equations

J. G. Zhou, D. M. Causon, C. G. Mingham, and D. M. Ingram

Centre for Mathematical Modelling and Flow Analysis, The Manchester Metropolitan University, Manchester M1 5GD, United Kingdom
E-mail: J.G.Zhou@mmu.ac.uk

Received February 21, 2000; revised October 12, 2000

A novel scheme has been developed for data reconstruction within a Godunov-type method for solving the shallow-water equations with source terms. In contrast to conventional data reconstruction methods based on conservative variables, the water surface level is chosen as the basis for data reconstruction. This provides accurate values of the conservative variables at cell interfaces so that the fluxes can be accurately calculated with a Riemann solver. The main advantages are: (1) a simple centered discretization is used for the source terms; (2) the scheme is no more complicated than the conventional method for the homogeneous terms; (3) small perturbations in the water surface elevation can be accurately predicted; and (4) the method is generally suitable for both steady and unsteady shallow-water problems. The accuracy of the scheme has been verified by recourse to both steady and unsteady flow problems. Excellent agreement has been obtained between the numerical predictions and analytical solutions. The results indicate that the new scheme is accurate, simple, efficient, and robust.

Key Words: source terms; shallow-water equations; data reconstruction; high-resolution method; Godunov method; MUSCL scheme.

1. INTRODUCTION

The shallow-water equations have wide applications in ocean and hydraulic engineering: tidal flows in estuary and coastal water regions; bore wave propagation, the stationary hydraulic jump; and river, reservoir, and open channel flows, among others. Research on methods of solution of the shallow-water equations has received considerable attention in the past two decades. A number of finite-volume schemes of the Godunov type have been developed recently to solve the inviscid form of the shallow-water equations [1–4]. However, the inclusion of source terms, e.g., those terms relevant to bed topography and bed shear stress, is often necessary to permit the modeling of realistic problems. For example,

0021-9991/01 $35.00

modeling tidal flows in estuary and coastal water regions usually requires consideration of the bed topography. Applications of the inviscid form of the shallow-water equations without source terms are largely limited to shock wave, bore wave, and dam break scenarios. The shallow-water equations can be shown to fail to predict a hydraulic jump accurately if the bed shear stress terms are neglected. A simple and direct method for solving the equations with source terms is a fractional step method [5], in which the inhomogeneous form of the equations is split into sets of equations, i.e., a homogeneous equation and a set of ordinary differential equations that are solved individually during a computation as part of a sequence of term-by-term split operators. This method, however, provides relatively poor solutions for quasi-steady or steady problems [6]. Thus, the study of methods for solving the full shallow-water equations continues to receive attention. Recently, various workers have developed new Godunov-type methods for the shallow water equations with source terms. For example, in 1994, Bermudez and Vázquez [7] proposed an upwind method for the treatment of the bed slope term for an unsteady flow problem. This method significantly improved the accuracy of the numerical solution compared with earlier methods. Later, Vázquez-Cendón [8] applied the same idea to solve a wider range of flow problems including steady ones. The main drawback of this method is its complexity. LeVeque [6] developed a treatment for the bed slope source terms which balanced the source terms and flux gradients. This method is suitable for quasi-steady problems but is reported to be less successful when applied to calculate steady transcritical flow with a shock.

In this paper, we propose the surface gradient method (SGM)—a general scheme for treating source terms in the shallow-water equations based on an accurate reconstruction of the conservative variables at cell interfaces. The fluxes at cell faces can then be accurately calculated with a Riemann solver without the need for term-by-term splitting. The standard Godunov-type method applied to the homogeneous form of the equations is recovered if the source terms are neglected. The SGM is applied to steady and unsteady shallow water problems involving bed slope terms to demonstrate both the accuracy and the applicability of the SGM.

2. 2D SHALLOW-WATER EQUATIONS

The 2D shallow-water equations with source terms may be written in vector form as

$$\frac{\partial \mathbf{U}}{\partial t} + \nabla \cdot \mathbf{F} = \mathbf{S}, \tag{1}$$

where $\mathbf{U}$ is the vector of conserved variables, $\mathbf{F}$ is the flux vector function, $\mathbf{S}$ is the vector of source terms, and $\nabla = \mathbf{i}\frac{\partial}{\partial x} + \mathbf{j}\frac{\partial}{\partial y}$ is the gradient operator. $\mathbf{U}$ and $\mathbf{F}$ are

$$\mathbf{U} = \begin{pmatrix} \phi \\ \phi u \\ \phi v \end{pmatrix}, \qquad \mathbf{F} = \begin{pmatrix} \phi \mathbf{V} \\ \phi u \mathbf{V} + \frac{1}{2}\phi^2 \mathbf{i} \\ \phi v \mathbf{V} + \frac{1}{2}\phi^2 \mathbf{j} \end{pmatrix} \tag{2}$$

and $\mathbf{S} = \mathbf{S}_b + \mathbf{S}_f$ with

$$\mathbf{S}_b = \begin{pmatrix} 0 \\ g\phi \frac{\partial H}{\partial x} \\ g\phi \frac{\partial H}{\partial y} \end{pmatrix}, \qquad \mathbf{S}_f = \begin{pmatrix} 0 \\ -\frac{g}{\rho}\tau_{fx} \\ -\frac{g}{\rho}\tau_{fy} \end{pmatrix}, \tag{3}$$

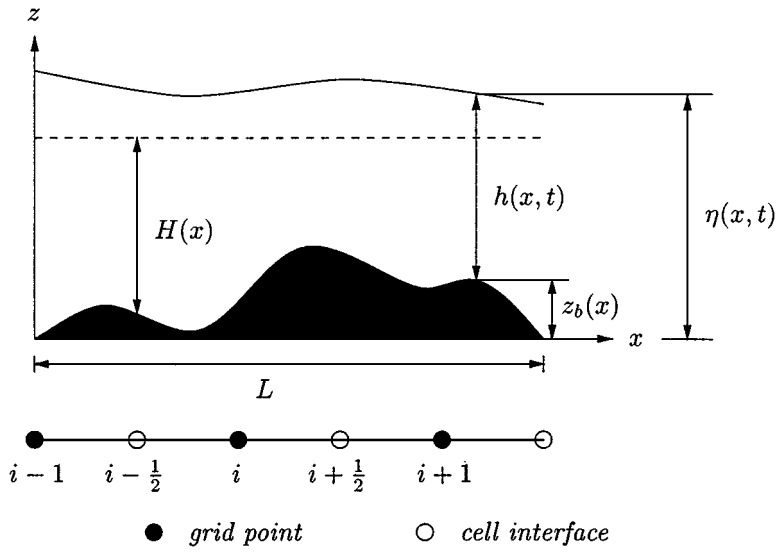

FIG. 1. Definition sketch for bed topography.

where $\phi = gh$ is the geopotential; $g = 9.81$ m/s^2 is the acceleration due to gravity; ρ is the water density; h is the water depth; H is the partial depth between a fixed reference level and the bed surface (see definition sketch in Fig. 1 for the 1D case); u and v are the x and y components of flow velocity, respectively; $\mathbf{V}$ is the velocity vector defined by $\mathbf{V} = u\mathbf{i} + v\mathbf{j}$; $\mathbf{S}_b$ is the bed slope term; and $\mathbf{S}_f$ is the bed shear stress term, with x and y components defined by depth-averaged velocities

$$\tau_{fx} = \rho C_f u\sqrt{u^2 + v^2}, \qquad \tau_{fy} = \rho C_f v\sqrt{u^2 + v^2}, \tag{4}$$

where C_f is the bed friction coefficient, which may either be constant or estimated from $C_f = g/C_z^2$, where C_z is the Chezy constant.

3. THE SURFACE GRADIENT METHOD (SGM)

An accurate data reconstruction scheme is proposed for the 2D shallow-water equations. For clarity, the following description will be restricted to the x direction. The same procedure can similarly be applied to the y direction and need not be repeated here.

To solve the continuity equation, fluxes based on the conservative variables are required at the cell interface. In higher order accurate Godunov-type methods, the values of the conservative variables within a cell are calculated using a reconstruction method based on the cell center data. Usually, a piecewise linear reconstruction is used, leading to a second order scheme, e.g., for ϕ within the cell i (Fig. 1)

$$\phi = \phi_i + (x - x_i)\delta\phi_i, \tag{5}$$

where $\delta\phi_i$ is the gradient of ϕ calculated by

$$\delta\phi_i = G\left(\frac{\phi_{i+1} - \phi_i}{x_{i+1} - x_i}, \frac{\phi_i - \phi_{i-1}}{x_i - x_{i-1}}\right), \tag{6}$$

in which G is a slope limiter which is used to avoid generating spurious oscillations in the reconstructed data at the cell interfaces [5]. The slope limiter may take one of several forms:

- minmod Limiter

$$G(a, b) = \max[0, \min(a, b)] \tag{7}$$

- van Leer Limiter

$$G(a, b) = \frac{a|b| + |a|b}{|a| + |b|} \tag{8}$$

- superbee Limiter

$$G(a, b) = s \max[0, \min(2|b|, sa), \min(|b|, 2sa)] \tag{9}$$

with $s = \text{sgn}(b)$.

The values of ϕ on the left and right of the cell interface $(i - \frac{1}{2})$ are

$$\phi^L_{i-\frac{1}{2}} = \phi_{i-1} + \frac{1}{2}\Delta x_{i-1}\delta\phi_{i-1}, \qquad \phi^R_{i-\frac{1}{2}} = \phi_i - \frac{1}{2}\Delta x_i \delta\phi_i, \tag{10}$$

where $\Delta x_i = x_{i+\frac{1}{2}} - x_{i-\frac{1}{2}}$ and

$$x_{i-\frac{1}{2}} = x_i - \frac{\Delta x_i}{2}, \qquad x_{i+\frac{1}{2}} = x_i + \frac{\Delta x_i}{2}. \tag{11}$$

It is clear that the gradient decided with Eq. (6) for the geopotential, ϕ, is effectively the gradient in depth, h, since $\phi = gh$. This method of data reconstruction, suitable for the homogeneous, or inviscid, form of the equations, is referred to hereafter as the depth gradient method (DGM). However, since we wish to include the effects of bed slope, the water depth at a cell interface will be influenced by the bed topography, in addition to variations in the free surface with time. In general, no matter what higher order accurate reconstruction method for water depth is applied, the depth at the cell interface cannot accurately be determined by this method. This is because the depth gradient fails to reproduce the real variation in water depth. Hence, errors introduced by the depth gradient method give rise to inaccurate fluxes which in turn produce inaccurate solutions. This can be clearly seen from Fig. 1. Values of water depth reconstructed using Eq. (10) are no longer exact at the cell interface even at the start of the computation. Such errors will be carried forward through the entire computation and are responsible for inaccuracies in the solution when bed slope source terms are included. For this reason many high-resolution Godunov-type methods fail to solve the shallow-water equations accurately when a centered discretization is used for the bed slope terms.

Since an accurate value of the conservative variable ϕ cannot be obtained at a cell interface with the depth gradient method, a new reconstruction scheme, the surface gradient method (SGM), is proposed. The water surface level $\eta(x, t)$ is defined as

$$\eta(x, t) = h(x, t) + z_b(x) \tag{12}$$

(see Fig. 1).

Following a similar approach, if a piecewise linear reconstruction is used for η, i.e.,

$$\eta = \eta_i + (x - x_i)\delta\eta_i, \tag{13}$$

the water levels at the left and right of the cell interface $(i - \frac{1}{2})$ are given by

$$\eta^{\mathrm{L}}_{i-\frac{1}{2}} = \eta_{i-1} + \frac{1}{2}\Delta x_{i-1}\delta\eta_{i-1}, \qquad \eta^{\mathrm{R}}_{i-\frac{1}{2}} = \eta_i - \frac{1}{2}\Delta x_i\delta\eta_i, \tag{14}$$

where $\delta\eta_i$ is the gradient of η within cell i (Fig. 1), which can be determined in exactly the same manner as $\delta\phi_i$.

The values of ϕ at the left and right of the cell interface $(i - \frac{1}{2})$ are then calculated as

$$\phi^{\mathrm{L}}_{i-\frac{1}{2}} = g\left(\eta^{\mathrm{L}}_{i-\frac{1}{2}} - z_{bi-\frac{1}{2}}\right), \qquad \phi^{\mathrm{R}}_{i-\frac{1}{2}} = g\left(\eta^{\mathrm{R}}_{i-\frac{1}{2}} - z_{bi-\frac{1}{2}}\right). \tag{15}$$

As can be seen from Eqs. (12)–(15), accurate values of the conservative variable ϕ at the cell interface can be determined with the surface gradient method, thus eliminating depth-related errors in computations of the fluxes at cell interfaces with the Riemann solver. The SGM is the same as the DGM in the absence of bed slope terms. It involves an equivalent level of computation effort to the DGM. When using the surface gradient method, the bed slope source term should be discretized with a centered scheme, as discussed in detail in Section 5. This leads to a particularly simple and efficient implementation of the method.

The new data reconstruction scheme remains fully conservative. This can be shown as follows: the depth within the cell i is

$$h(x,t) = \eta(x,t) - z_b(x) = \eta_i + (x - x_i)\delta\eta_i - z_b(x). \tag{16}$$

Integration of Eq. (16) over the interval $(x_{i-\frac{1}{2}}, x_{i+\frac{1}{2}})$ gives

$$\int_{x_{i-\frac{1}{2}}}^{x_{i+\frac{1}{2}}} h(x,t)\,dx = \int_{x_{i-\frac{1}{2}}}^{x_{i+\frac{1}{2}}} \eta_i\,dx + \int_{x_i-\frac{1}{2}}^{x_{i+\frac{1}{2}}} (x - x_i)\,\delta\eta_i\,dx - \int_{x_i-\frac{1}{2}}^{x_{i+\frac{1}{2}}} z_b(x)\,dx, \tag{17}$$

which can be simplified to

$$\frac{1}{\Delta x_i}\int_{x_{i-\frac{1}{2}}}^{x_{i+\frac{1}{2}}} h(x,t)\,dx = \eta_i - \frac{1}{\Delta x_i}\int_{x_{i-\frac{1}{2}}}^{x_{i+\frac{1}{2}}} z_b(x)\,dx. \tag{18}$$

If the bed topography is defined at cell interfaces and a piecewise linear profile for z_b within the cell is assumed, z_b at the cell center is then expressed exactly as

$$z_{bi} = \frac{z_{bi+\frac{1}{2}} + z_{bi-\frac{1}{2}}}{2}. \tag{19}$$

The second term on the right-hand side of Eq. (18) can be accurately calculated; i.e.,

$$\int_{x_{i-\frac{1}{2}}}^{x_{i+\frac{1}{2}}} z_b(x)\,dx = \left(z_{bi+\frac{1}{2}} + 2z_{bi} + z_{bi-\frac{1}{2}}\right)\frac{\Delta x_i}{4} = z_{bi}\,\Delta x_i. \tag{20}$$

Substitution of Eq. (20) into Eq. (18) results in

$$\frac{1}{\Delta x_i}\int_{x_{i-\frac{1}{2}}}^{x_{i+\frac{1}{2}}} h(x,t)\,dx = \eta_i - z_{bi} = h_i, \tag{21}$$

which shows that the depth at cell center i is retained as the integral average over the interval $(x_{i-1/2}, x_{i+1/2})$, consistent with the conventional depth gradient method, confirming that the scheme is conservative [9].

4. IMPLEMENTATION WITHIN A GODUNOV-TYPE METHOD

The surface gradient method can be incorporated into any Godunov-type method which requires data reconstruction. Here, the MUSCL–Hancock finite-volume method [10] is applied to the solution of Eq. (1). The method is a second-order-accurate, high-resolution, upwind scheme of the Godunov type. It consists of two steps: a predictor step and a corrector step.

In the predictor step, a nonconservative approach is used to determine the intermediate values over a half time step,

$$(A\mathbf{U})_{ij}^{n+\frac{1}{2}} = (A\mathbf{U})_{ij}^{n} - \frac{\Delta t}{2}\left(\sum_{m=1}^{M}\mathbf{F}(\mathbf{U}_m)^n\cdot\mathbf{L}_m - (A\mathbf{S})_{ij}^{n}\right), \tag{22}$$

where A is the cell area, $\mathbf{L}_m$ is the cell side vector defined as the cell side length multiplied by the outward pointing unit normal vector, and $M = 4$ is the number of sides of the cell. The flux vector $\mathbf{F}(\mathbf{U}_m)$ is evaluated at each cell face m following data reconstruction based on neighboring cell center data. For the continuity equation, the SGM is used; i.e., the values of ϕ at the cell interfaces $(i-\frac{1}{2}j)$ and $(i+\frac{1}{2}j)$ for the cell ij under consideration are expressed using Eq. (15) as

$$\phi_{i-\frac{1}{2}j} = g\big(\eta_{i-\frac{1}{2}j} - z_{bi-\frac{1}{2}j}\big), \qquad \phi_{i+\frac{1}{2}j} = g\big(\eta_{i+\frac{1}{2}j} - z_{bi+\frac{1}{2}j}\big), \tag{23}$$

where

$$\eta_{i-\frac{1}{2}j} = \eta_{ij} - \frac{1}{2}\Delta x_{ij}\delta\eta_{xij}, \qquad \eta_{i+\frac{1}{2}j} = \eta_{ij} + \frac{1}{2}\Delta x_{ij}\delta\eta_{xij}. \tag{24}$$

For the momentum equations, a piecewise linear reconstruction is used to calculate the values of ϕu and ϕv at cell interfaces. For example, ϕu and ϕv at the cell interfaces $(i-\frac{1}{2}j)$ and $(i+\frac{1}{2}j)$ can be calculated as

$$(\phi u)_{i-\frac{1}{2}j} = (\phi u)_{ij} - \frac{1}{2}\Delta x_{ij}\delta(\phi u)_{xij}, \tag{25}$$

$$(\phi u)_{i+\frac{1}{2}j} = (\phi u)_{ij} + \frac{1}{2}\Delta x_{ij}\delta(\phi u)_{xij} \tag{26}$$

and

$$(\phi v)_{i-\frac{1}{2}j} = (\phi v)_{ij} - \frac{1}{2}\Delta x_{ij}\delta(\phi v)_{xij}, \tag{27}$$

$$(\phi v)_{i+\frac{1}{2}j} = (\phi v)_{ij} + \frac{1}{2}\Delta x_{ij}\delta(\phi v)_{xij}, \tag{28}$$

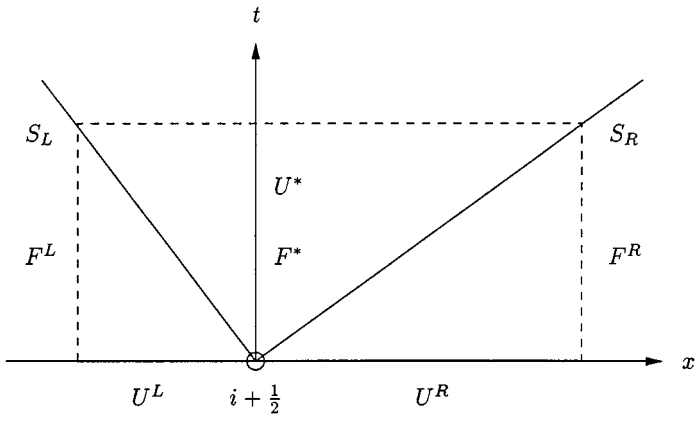

FIG. 2. HLL approximate Riemann solver.

where $\delta(\phi u)_{xij}$ and $\delta(\phi v)_{xij}$ are the gradients of ϕu and ϕv in the x direction within the cell ij, respectively. They are calculated in the same way as $\delta\phi_i$.

In the corrector step, a fully conservative solution over a full time step is achieved by solving a series of local Riemann problems based on data from the predictor step,

$$(A\mathbf{U})_{ij}^{n+1} = (A\mathbf{U})_{ij}^{n} - \Delta t\left(\sum_{m=1}^{M}\mathbf{F}\left(\mathbf{U}_m^{\mathrm{L}}, \mathbf{U}_m^{\mathrm{R}}\right)^{n+\frac{1}{2}}\cdot\mathbf{L}_m - (A\mathbf{S})_{ij}^{n+\frac{1}{2}}\right), \tag{29}$$

where the flux vector $\mathbf{F}(\mathbf{U}_m^{\mathrm{L}}, \mathbf{U}_m^{\mathrm{R}})$ is calculated by solving a local Riemann problem at each cell interface. $\mathbf{U}_m^{\mathrm{L}}$ and $\mathbf{U}_m^{\mathrm{R}}$ are vectors of the conservative variables at the left and right sides of cell interface m, defined by expressions such as Eq. (15) for ϕ and expressions similar to Eqs. (25), (26) and Eqs. (27), (28) for ϕu and ϕv, respectively. Although different Riemann solvers may be used for $\mathbf{F}(\mathbf{U}_m^{\mathrm{L}}, \mathbf{U}_m^{\mathrm{R}})$, the HLL approximate Riemann solver [11] is found to be simpler to implement and more robust in practice. Hence, it is used in the present study. In the HLL Riemann solver, the Riemann problem is simplified as three constant states separated by two waves s_{L} and s_{R} between which it is the star region as shown in Fig. 2. The flux at the cell interface $i+\frac{1}{2}$ is determined by

$$\mathbf{F}\left(\mathbf{U}_m^{\mathrm{L}}, \mathbf{U}_m^{\mathrm{R}}\right) = \begin{cases} \mathbf{F}\left(\mathbf{U}_m^{\mathrm{L}}\right) & \text{if } s_{\mathrm{L}} \geq 0 \\ \mathbf{F}^*\left(\mathbf{U}_m^{\mathrm{L}}, \mathbf{U}_m^{\mathrm{R}}\right) & \text{if } s_{\mathrm{L}} < 0 < s_{\mathrm{R}} \\ \mathbf{F}\left(\mathbf{U}_m^{\mathrm{R}}\right) & \text{if } s_{\mathrm{R}} \leq 0, \end{cases} \tag{30}$$

where

$$\mathbf{F}^*\left(\mathbf{U}_m^{\mathrm{L}}, \mathbf{U}_m^{\mathrm{R}}\right) = \frac{s_{\mathrm{R}}\mathbf{F}\left(\mathbf{U}_m^{\mathrm{L}}\right) - s_{\mathrm{L}}\mathbf{F}\left(\mathbf{U}_m^{\mathrm{R}}\right) + s_{\mathrm{L}}s_{\mathrm{R}}\left(\mathbf{U}_m^{\mathrm{R}} - \mathbf{U}_m^{\mathrm{L}}\right)}{s_{\mathrm{R}} - s_{\mathrm{L}}} \tag{31}$$

with wave speeds s_{L} and s_{R} defined by

$$s_{\mathrm{L}} = \min(\mathbf{V}^{\mathrm{L}}\cdot\mathbf{n}_m - \sqrt{\phi^{\mathrm{L}}}, u_s - \sqrt{\phi_s}), \tag{32}$$

$$s_{\mathrm{R}} = \max(\mathbf{V}^{\mathrm{R}}\cdot\mathbf{n}_m + \sqrt{\phi^{\mathrm{R}}}, u_s + \sqrt{\phi_s}) \tag{33}$$

in which u_s and ϕ_s are estimated as [12]

$$u_s = \frac{1}{2}(\mathbf{V}^{\mathrm{L}} + \mathbf{V}^{\mathrm{R}}) \cdot \mathbf{n}_m + \sqrt{\phi^{\mathrm{L}}} - \sqrt{\phi^{\mathrm{R}}}, \tag{34}$$

$$\sqrt{\phi_s} = \frac{\sqrt{\phi^{\mathrm{L}}} + \sqrt{\phi^{\mathrm{R}}}}{2} + \frac{(\mathbf{V}^{\mathrm{L}} - \mathbf{V}^{\mathrm{R}}) \cdot \mathbf{n}_m}{4}, \tag{35}$$

and $\mathbf{n}_m$ is the normalized side vector for cell face m.

It may be noted that the expressions (32) and (33) for a dry bed problem are modified as [13]

$$s_{\mathrm{L}} = \mathbf{V}^{\mathrm{L}} \cdot \mathbf{n}_m - \sqrt{\phi^{\mathrm{L}}}, \qquad s_{\mathrm{R}} = \mathbf{V}^{\mathrm{L}} \cdot \mathbf{n}_m + 2\sqrt{\phi^{\mathrm{L}}} \quad \text{(right dry bed)} \tag{36}$$

and

$$s_{\mathrm{L}} = \mathbf{V}^{\mathrm{R}} \cdot \mathbf{n}_m - 2\sqrt{\phi^{\mathrm{R}}}, \qquad s_{\mathrm{R}} = \mathbf{V}^{\mathrm{R}} \cdot \mathbf{n}_m + \sqrt{\phi^{\mathrm{R}}} \quad \text{(left dry bed)}. \tag{37}$$

Although the SGM proposed in Section 3 is generally suitable for both uniform and nonuniform meshes, a uniform Cartesian mesh is used here to maintain the same computational conditions as reported in the literature. The time step Δt is calculated at the start of each time step by

$$\Delta t = C_t \ \min(\Delta t_x, \Delta t_y), \tag{38}$$

where

$$\Delta t_x = \min_i \frac{\Delta x}{u_{ij} + \sqrt{\phi_{ij}}}, \qquad \Delta t_y = \min_j \frac{\Delta y}{v_{ij} + \sqrt{\phi_{ij}}} \tag{39}$$

in which C_t is the Courant number ($0 < C_t \leq 1$). To test the robustness of the scheme, three values, 0.3, 0.65, and 1, were used for C_t in all the numerical computations presented here, and no stability problem was encountered.

5. CONSERVATIVE PROPERTY AND SOURCE TERMS

5.1. *Conservative Property*

It is well known that for a stationary flow problem,

$$h \equiv H, \qquad \mathbf{V} \equiv 0, \tag{40}$$

there are nonvanishing terms in the momentum equations owing to bed topography, i.e.,

$$\frac{\partial}{\partial x}\left(\frac{1}{2}\phi^2\right) = g\phi\frac{\partial H}{\partial x}, \qquad \frac{\partial}{\partial y}\left(\frac{1}{2}\phi^2\right) = g\phi\frac{\partial H}{\partial y}. \tag{41}$$

If a numerical scheme can replicate the exact solution to the stationary flow problem (40), the scheme is said to satisfy the exact $\mathcal{C}$-property [7, 14].

DEFINITION 5.1. $\mathcal{Z}$-property: (i) a numerical scheme provides the exact values of a variable in the flow domain to the stationary case $h \equiv H$, $\mathbf{V} \equiv 0$; (ii) the scheme satisfies the exact $\mathcal{C}$-property when a centered discretiztion is used for source terms.

PROPOSITION 5.1. *The numerical scheme proposed in Section* 3 *satisfies the* $\mathcal{Z}$*-property.*

Proof. Without loss of generality, only the one-dimensional situation is considered here. The proof for two-dimensional problems can be formulated in an analogous manner. For the initial stationary problem (40), the wave speeds from Eqs. (32) and (33) are

$$s_{\mathrm{L}} = -\sqrt{gh}, \qquad s_{\mathrm{R}} = \sqrt{gh}. \tag{42}$$

In the predictor step, the x component of numerical flux, F_x, is

$$F_x = \frac{\left[\phi\left(u^2 + \frac{1}{2}\phi\right)\right]_{i+\frac{1}{2}} - \left[\phi\left(u^2 + \frac{1}{2}\phi\right)\right]_{i-\frac{1}{2}}}{\Delta x} = \frac{1}{2}g^2 \frac{\left(h_{i+\frac{1}{2}} + h_{i-\frac{1}{2}}\right)\left(h_{i+\frac{1}{2}} - h_{i-\frac{1}{2}}\right)}{\Delta x} \tag{43}$$

because $u \equiv 0$ and $\phi = gh$.

It should be noted that the water level is constant under the initial condition $h \equiv H$ and $u \equiv 0$. Data reconstruction with the surface gradient method provides zero gradient ($\delta\eta = 0$) for the water level in the whole domain; hence the method gives the exact values of depth h or ϕ in the whole domain. According to Eqs. (23) and (24),

$$h_{i-\frac{1}{2}} = \eta_{i-\frac{1}{2}} - z_{bi-\frac{1}{2}} = \eta_i - \frac{1}{2}\Delta x \delta\eta_i - z_{bi-\frac{1}{2}} \tag{44}$$

$$h_{i+\frac{1}{2}} = \eta_{i+\frac{1}{2}} - z_{bi+\frac{1}{2}} = \eta_i + \frac{1}{2}\Delta x \delta\eta_i - z_{bi+\frac{1}{2}}, \tag{45}$$

we have

$$\frac{\left(h_{i+\frac{1}{2}} + h_{i-\frac{1}{2}}\right)}{2} = \eta_i - \frac{\left(z_{bi+\frac{1}{2}} + z_{bi-\frac{1}{2}}\right)}{2} = (\eta_i - z_{bi}) + z_{bi} - \frac{\left(z_{bi+\frac{1}{2}} + z_{bi-\frac{1}{2}}\right)}{2}. \tag{46}$$

Noting that $(\eta_i - z_{bi}) = h_i$ and $z_{bi} - (z_{bi+1/2} + z_{bi-1/2})/2 = 0$ if the bed level z_b is defined at the cell interfaces, Eq. (46) becomes

$$\frac{\left(h_{i+\frac{1}{2}} + h_{i-\frac{1}{2}}\right)}{2} = h_i. \tag{47}$$

Substitution of Eq. (47) into Eq. (43) results in

$$F_x = g^2 h_i \frac{\left(h_{i+\frac{1}{2}} - h_{i-\frac{1}{2}}\right)}{\Delta x}. \tag{48}$$

At the same time, the x component of the bed slope source term is

$$S_x = g\phi_i \frac{H_{i+\frac{1}{2}} - H_{i-\frac{1}{2}}}{\Delta x} = g^2 h_i \frac{h_{i+\frac{1}{2}} - h_{i-\frac{1}{2}}}{\Delta x} = F_x \tag{49}$$

because $h \equiv H$. This proves that the numerical scheme in the predictor step satisfies the exact $\mathcal{C}$-property; hence $h \equiv H$ and $u \equiv 0$ are preserved after the predictor step.

In the corrector step, the numerical flux at the right-hand interface, $F_{i+1/2}$ is defined by Eq. (30),

$$F_{i+\frac{1}{2}} = \frac{s_{\mathrm{R}}\left[\phi\left(u^2+\frac{1}{2}\phi\right)\right]^{\mathrm{L}}_{i+\frac{1}{2}} - s_{\mathrm{L}}\left[\phi\left(u^2+\frac{1}{2}\phi\right)\right]^{\mathrm{R}}_{i+\frac{1}{2}} + s_{\mathrm{L}}s_{\mathrm{R}}\left[(\phi u)^{\mathrm{R}}_{i+\frac{1}{2}} - (\phi u)^{\mathrm{L}}_{i+\frac{1}{2}}\right]}{s_{\mathrm{R}} - s_{\mathrm{L}}}, \quad (50)$$

because $s_{\mathrm{L}} < 0 < s_{\mathrm{R}}$.

Since up to this point $h \equiv H$ and $u \equiv 0$ will have been maintained over the whole domain, ϕ can be obtained exactly with the surface gradient method and no discontinuity in water depth will appear anywhere in the domain; i.e., $\phi^{\mathrm{L}} \equiv \phi^{\mathrm{R}}$ at all the cell interfaces. Substitution of the wave speeds (42) and $u \equiv 0$ into the above equation gives

$$F_{i+\frac{1}{2}} = \frac{\frac{1}{2}\sqrt{gh_{i+\frac{1}{2}}}\phi^2_{i+\frac{1}{2}} + \frac{1}{2}\sqrt{gh_{i+\frac{1}{2}}}\phi^2_{i+\frac{1}{2}}}{2\sqrt{gh_{i+\frac{1}{2}}}} = \frac{1}{2}\phi^2_{i+\frac{1}{2}}. \quad (51)$$

Similarly, we have

$$F_{i-\frac{1}{2}} = \frac{1}{2}\phi^2_{i-\frac{1}{2}}. \quad (52)$$

The numerical flux is

$$F_x = \frac{F_{i+\frac{1}{2}} - F_{i-\frac{1}{2}}}{\Delta x} = \frac{\frac{1}{2}\phi^2_{i+\frac{1}{2}} - \frac{1}{2}\phi^2_{i-\frac{1}{2}}}{\Delta x} = \frac{1}{2}g^2\frac{\left(h_{i+\frac{1}{2}} + h_{i-\frac{1}{2}}\right)\left(h_{i+\frac{1}{2}} - h_{i-\frac{1}{2}}\right)}{\Delta x}, \quad (53)$$

which has exactly the same form as Eq. (43) in the predictor step with the same initial conditions (40). It then follows that the corrector step also satisfies the exact $\mathcal{C}$-property. The importance of a scheme satisfying the $\mathcal{C}$-property has been demonstrated by Bermudez and Vázquez [7]. Again, $h \equiv H$ and $u \equiv 0$ are preserved after the corrector step.

Therefore, the numerical scheme satisfies the $\mathcal{Z}$-property. ■

5.2. *Discretization of Source Terms*

As discussed in the previous section, no special treatment is needed for the discretization of the source terms when using the data reconstruction scheme described in Section 3. In fact, a centered discretization is applied for the source terms to retain the conservative property. For example, the bed slope term at cell ij is discretized as

$$\iint_{\Delta x\Delta y} g\phi\frac{\partial H}{\partial x}\,dx\,dy = g\phi_{ij}\left(H_{i+\frac{1}{2}j} - H_{i-\frac{1}{2}j}\right)\Delta y, \quad (54)$$

which gives second-order accuracy.

6. VERIFICATION OF THE SCHEME

In this section, the proposed scheme is verified by solving some benchmark problems including both steady and unsteady flows. The accuracy is demonstrated by comparing the numerical solutions with analytical solutions, available numerical results, and experimental

data. To replicate the computational conditions reported in the literature, the bed slope source term is always taken into account and the bed friction terms are omitted except in the test problem in Section 6.5, which applies the method to the treatment of bed friction terms.

6.1. *Tidal Wave Flow*

Tidal waves often have to be considered in coastal engineering. Here we consider the test problem that Bermudez and Vázquez [7] used for verification of an upwind discretization of the bed slope source terms. This is a one-dimensional problem with bed topography defined by (Fig. 3)

$$H(x) = 50.5 - \frac{40x}{L} - 10\sin\left[\pi\left(\frac{4x}{L} - \frac{1}{2}\right)\right], \tag{55}$$

where $L = 14{,}000$ m is the channel length. The initial and boundary conditions are

$$h(x, 0) = H(x), \tag{56}$$

$$u(x, 0) = 0 \tag{57}$$

and

$$h(0, t) = H(0) + 4 - 4\sin\left[\pi\left(\frac{4t}{86{,}400} + \frac{1}{2}\right)\right], \tag{58}$$

$$u(L, t) = 0. \tag{59}$$

Under these conditions, the tidal wave is relatively short and an asymptotic analytical solution is derived by Bermudez and Vázquez [7] as

$$h(x, t) = H(x) + 4 - 4\sin\left[\pi\left(\frac{4t}{86{,}400} + \frac{1}{2}\right)\right], \tag{60}$$

$$u(x, t) = \frac{(x - L)\pi}{5400h(x, t)}\cos\left[\pi\left(\frac{4t}{86{,}400} + \frac{1}{2}\right)\right]. \tag{61}$$

Without any further modifications, the 2D code can be directly applied to solve this tidal flow problem. In the computations, 50 nodes with $\Delta x = 280$ m, which is the same as that by Bermudez and Vázquez, were used. Equations (56)–(59) were used as the initial and boundary conditions.

A comparison of the numerical results with the asymptotic analytical solution at $t = 7552.13$ s is shown in Figs. 3 and 4. The agreement is excellent. This suggests that the proposed scheme is accurate for tidal flow problems. The present method provides predictions of the same accuracy as the scheme reported by Bermudez and Vázquez, which has a more complex upwind discretisation of the bed slope source terms [7].

6.2. *Tidal Wave Flow over an Irregular Bed*

To validate the method to solve the flow over an irregular bed, we present here a tidal flow over an irregular bed which was proposed at a workshop on dambreak wave simulations [15]. The same bed is also used by Vázquez–Cendón [8]. The bed topography is defined in Table I and shown in Fig. 6.

TABLE I
Bed Elevation at Point x for Irregular Bed

x	0	50	100	150	250	300	350	400	425	435	450	475	500	505
z_b	0	0	2.5	5	5	3	5	5	7.5	8	9	9	9.1	9
x	530	550	565	575	600	650	700	750	800	820	900	950	1000	1500
z_b	9	6	5.5	5.5	5	4	3	3	2.3	2	1.2	0.4	0	0

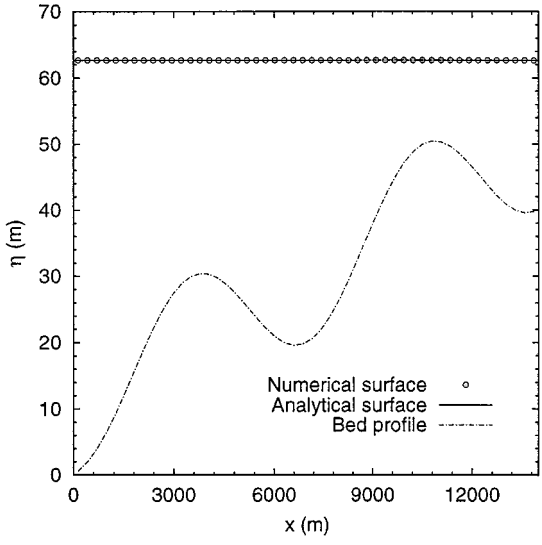

FIG. 3. Tidal wave flow: Comparison of water surface $\eta(x, t)$.

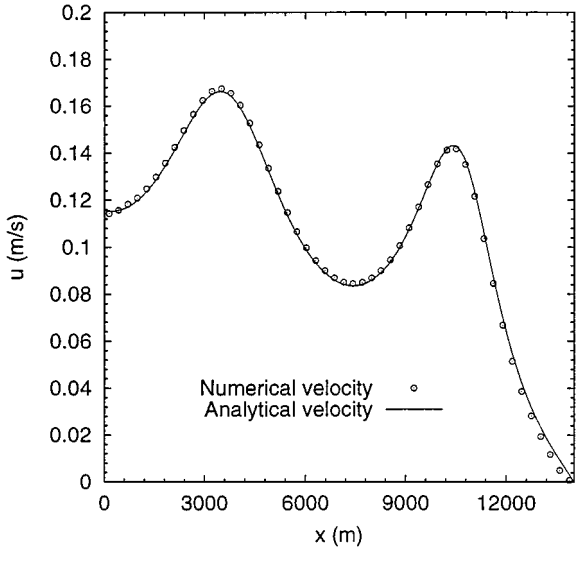

FIG. 4. Tidal wave flow: Comparison of velocity $u(x, t)$.

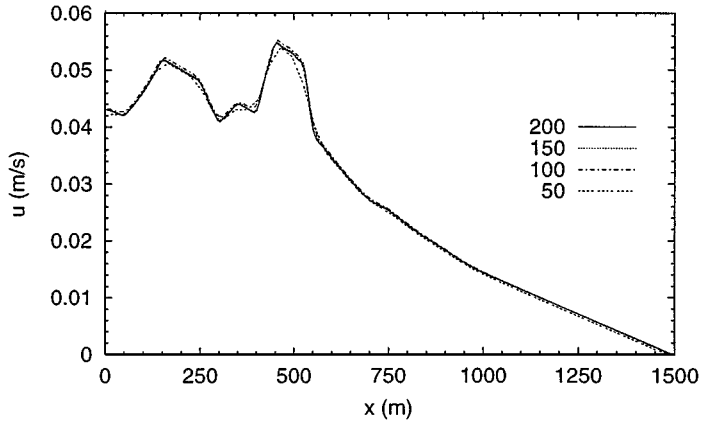

FIG. 5. Tidal wave flow over an irregular bed: Effect of mesh sizes.

The initial and boundary conditions are described by the same equations (56)–(59) as the problem in Section 6.1, but with

$$H(0) = 16 \text{ m}, \qquad L = 1500 \text{ m}, \qquad H(x) = H(0) - z_b(x). \tag{62}$$

Under these conditions, the tidal wave is also relatively short and an asymptotic analytical solution is then given by the same equations, (60) and (61).

In the numerical computations, four mesh sizes, i.e., 50, 100, 150, and 200 cells, were used to achieve a grid-independent solution. Comparisons of the maximum positive velocities at $t = 10{,}800$ s are shown in Fig. 5, corresponding to the half-risen tidal flow. It is clearly seen from the figure that the results based on 200 cells with $\Delta x = 7.5$ m can be regarded as a grid-independent solution used for the following presentation.

To compare the numerical results with the asymptotic analytical solution, we choose two results at $t = 10{,}800$ s and $t = 32{,}400$ s, which correspond to the half-risen tidal flow with maximum positive velocities and to the half-ebb tidal flow with maximum negative velocities. Figure 6 shows a comparison between the predicted surface and the analytical solution at $t = 10{,}800$ s. A comparison of velocities is depicted in Figs. 7 and 8. Excellent agreement is obtained between the numerical and the analytical solutions. This confirms that the proposed scheme is also accurate for tidal flow over an irregular bed.

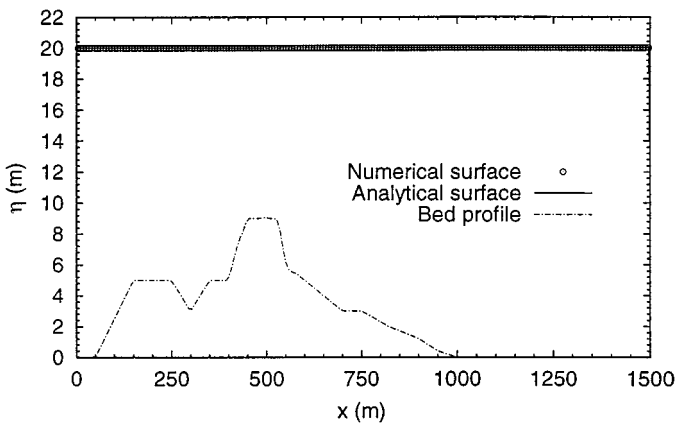

FIG. 6. Tidal wave flow over an irregular bed: Comparison of surfaces $\eta(x, t)$ at $t = 10{,}800$ s.

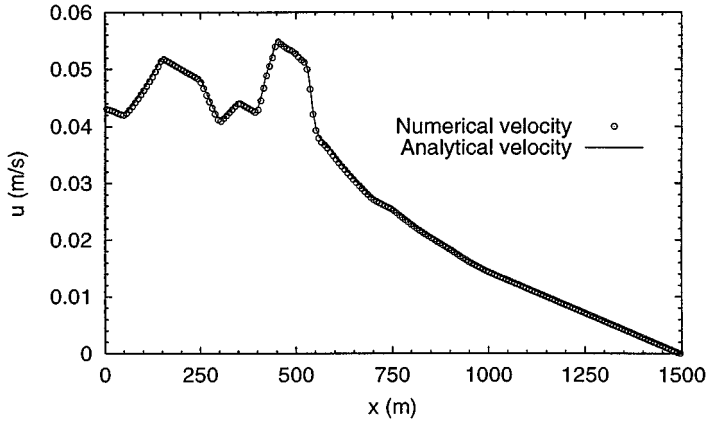

FIG. 7. Tidal wave flow over an irregular bed: Comparison of velocity $u(x, t)$ at $t = 10{,}800$ s.

6.3. *Steady Flow over a Bump*

A 1D steady flow in a 25-m-long channel with a bump defined by

$$z_b(x) = \begin{cases} 0.2 - 0.05(x - 10)^2 & \text{if } 8 < x < 12 \\ 0 & \text{otherwise} \end{cases} \tag{63}$$

is a classical test problem which has been used as a benchmark test case for numerical methods at the workshop on dam-break wave simulations [15]. The problem was also used by Vázquez-Cendón [8] to test their scheme with an upwind discretization for the bed slope source terms.

Depending on the initial and boundary conditions, the flow may be subcritical, transcritical with or without a steady shock, or supercritical. Analytical solutions for the various cases are given by Goutal [15].

The global relative error R is defined by

$$R = \sqrt{\sum_i \left(\frac{h_i^n - h_i^{n-1}}{h_i^n} \right)^2}, \tag{64}$$

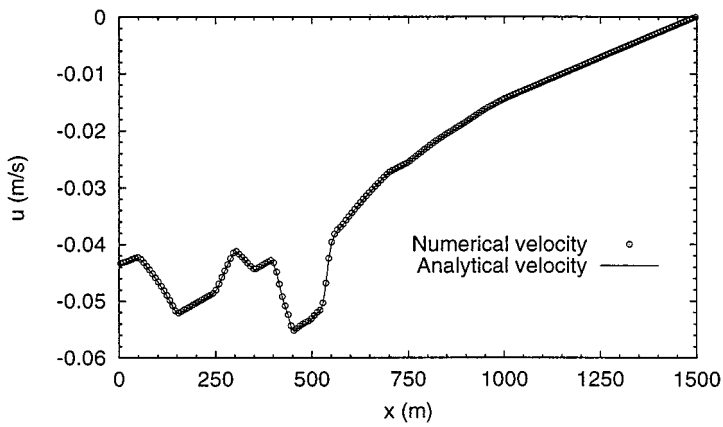

FIG. 8. Tidal wave flow over an irregular bed: Comparison of velocity $u(x, t)$ at $t = 32{,}400$ s.

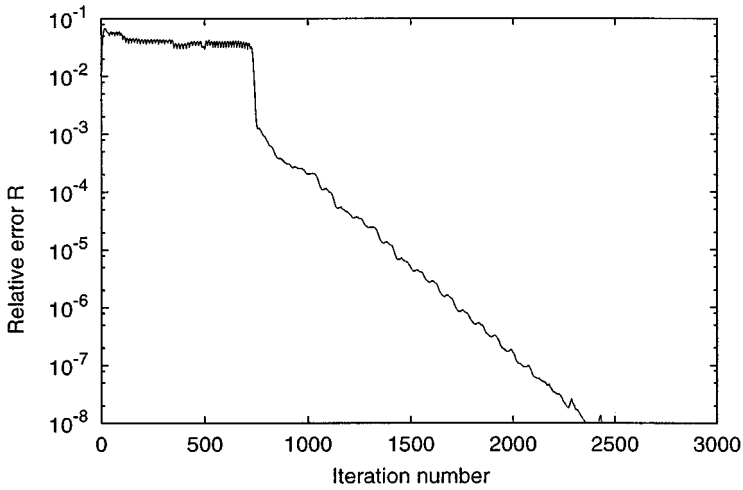

FIG. 9. Steady transcritical flow over a bump without a shock: Convergence history.

where h^n and h^{n-1} are the local water depths at the current and previous time levels. The convergence criterion for a steady solution is defined as $R < 5 \times 10^{-6}$.

Transcritical flow without a shock. The physical domain was partitioned with 100 cells and $\Delta x = 0.25$ m. A discharge per unit width of $q = 1.53\,\mathrm{m}^2/\mathrm{s}$ was imposed at the upstream boundary and no boundary condition was needed at the downstream end of the channel. A steady-state solution was reached after 1500 iterations, as is clearly shown in the convergence history (Fig. 9). The surface profile is plotted in Fig. 10, which shows very good agreement with the analytical solution. The computed discharge is also compared with the theoretical one in Fig. 11, which proves that the method is conservative.

Transcritical flow with a shock. In this case, a discharge per unit width of $q = 0.18\,\mathrm{m}^2/\mathrm{s}$ was imposed at the upstream boundary and $h = 0.33$ m was specified as the downstream boundary condition. To establish grid independence, three meshes of 100, 200, and 400 nodes were used. The convergent solutions are plotted in Fig. 12. Differences in the

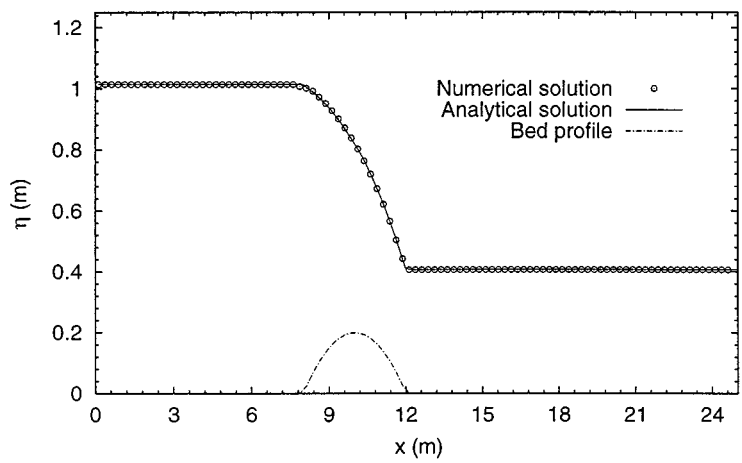

FIG. 10. Steady transcritical flow over a bump without a shock: Water surface elevation.

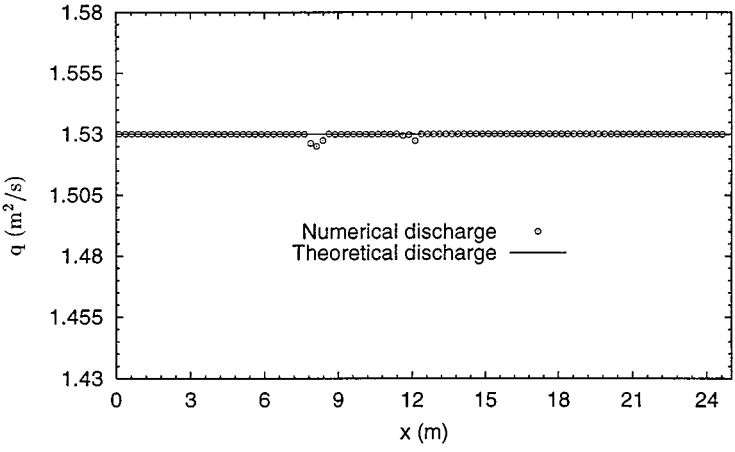

FIG. 11. Steady transcritical flow over a bump without a shock: Comparison of discharge.

results with 100 and 200 cells clearly exist within the shock region, but the results based on 200 and 400 cells are almost the same. Hence results based on the mesh with 200 cells were used for presentation here. A steady-state solution was reached after 2773 iterations. Figure 13 shows the numerical results and the analytical solution, where very good agreement has been obtained. In Fig. 14, the Froude number $Fr = u/\sqrt{gh}$ is compared with the theoretical values. Figures 15 and 16 show a comparison of the computed discharge with the theoretical results and the convergence history, respectively.

Subcritical flow. A mesh interval of $\Delta x = 0.25$ m was used in the computations. A discharge per unit width of $q = 4.42$ m^2/s was imposed at the upstream boundary and $h = 2$ m was specified as the downstream boundary condition. A steady-state solution was reached after 782 iterations. The numerical results are depicted in Figs. 17 and 18, which again show excellent agreement with the analytical solution. The convergence history is plotted in Fig. 19.

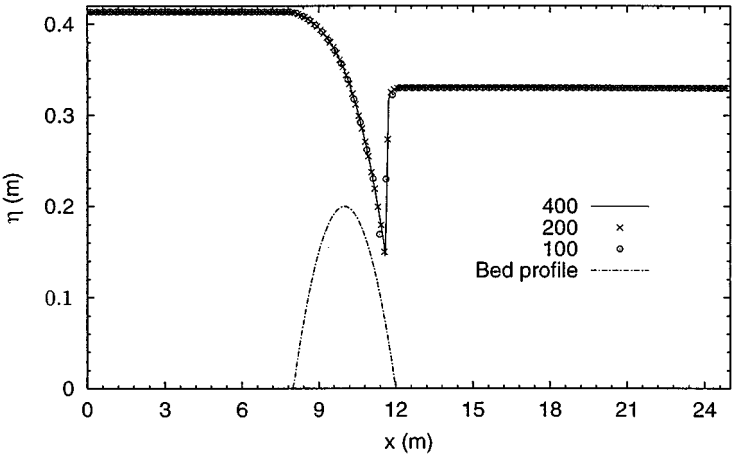

FIG. 12. Steady transcritical flow over a bump with a shock: Effect of mesh sizes.

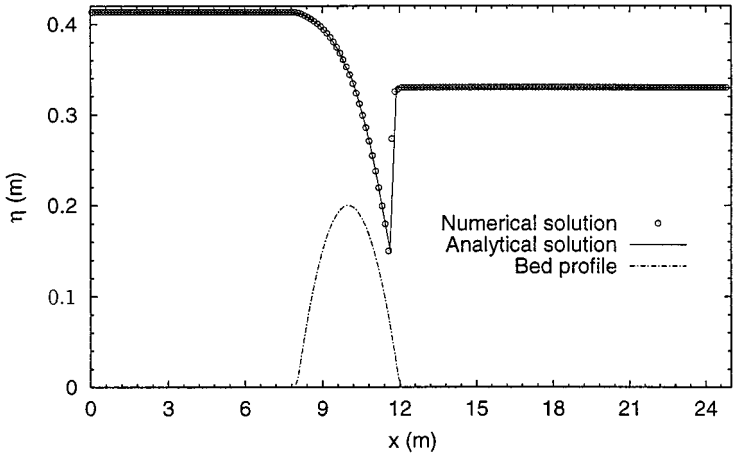

FIG. 13. Steady transcritical flow over a bump with a shock: Water surface elevation.

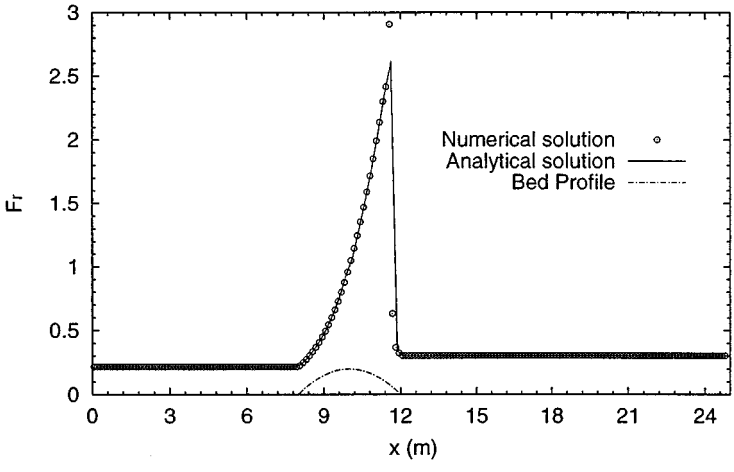

FIG. 14. Steady transcritical flow over a bump with a shock: Froude number.

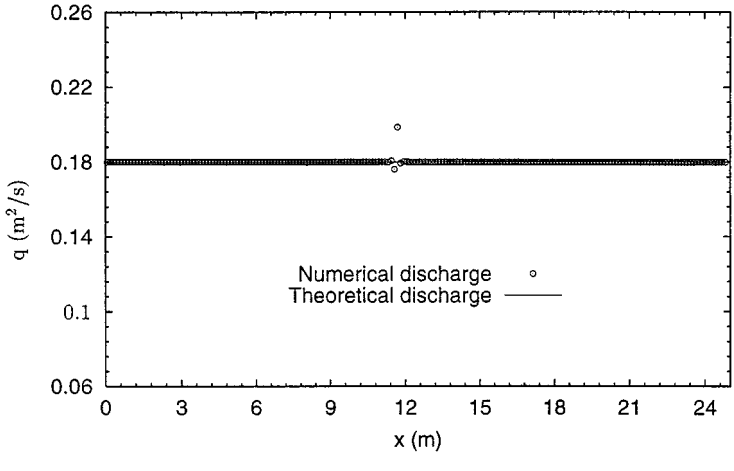

FIG. 15. Steady transcritical flow over a bump with a shock: Comparison of discharge.

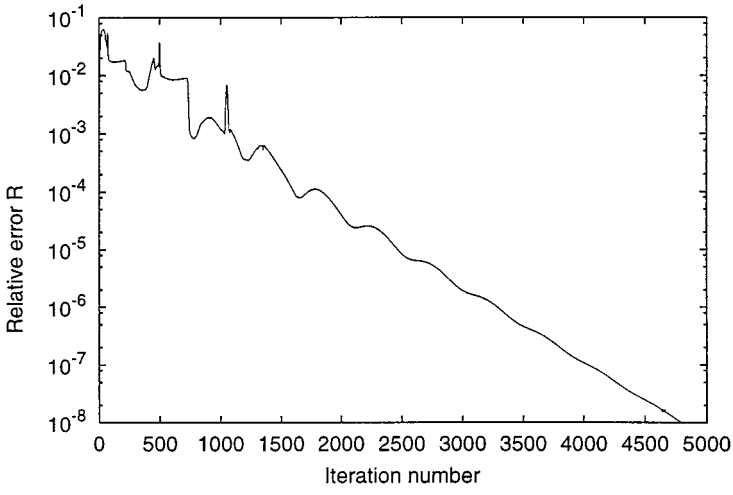

FIG. 16. Steady transcritical flow over a bump with a shock: Convergence history.

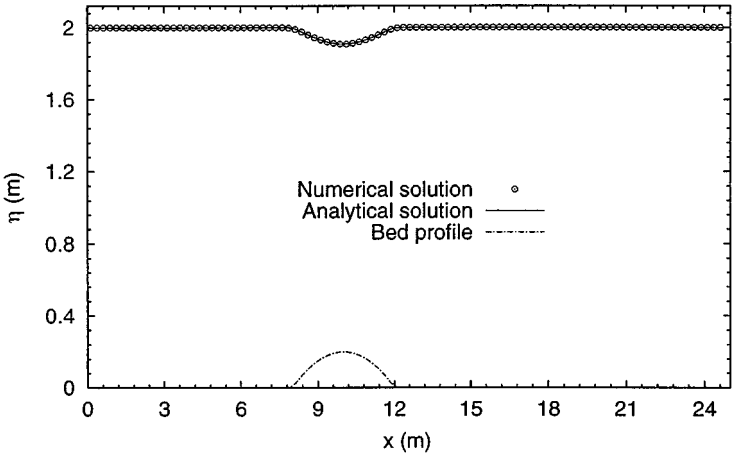

FIG. 17. Steady subcritical flow over a bump: Water surface elevation.

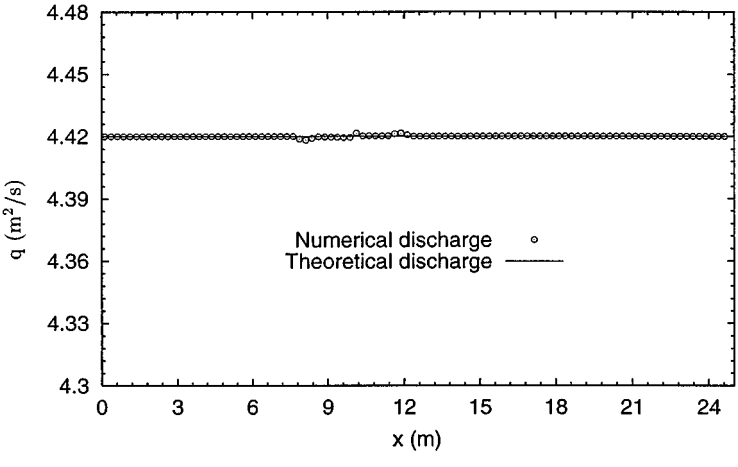

FIG. 18. Steady subcritical flow over a bump: Comparison of discharge.

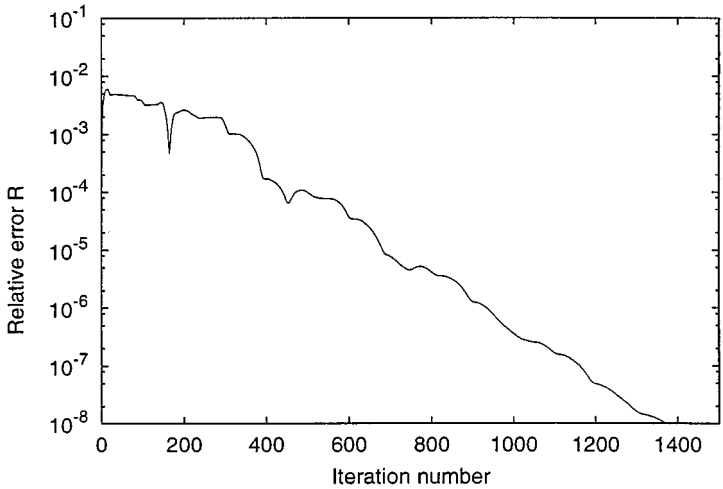

FIG. 19. Steady subcritical flow over a bump: Convergence history.

6.4. *A Quasi-stationary Case*

A quasi-stationary test case used by LeVeque [6] was chosen to demonstrate the capability of the proposed scheme for computations involving small perturbations of the water surface. The bed topography is

$$z_b(x) = \begin{cases} 0.25[\cos(\pi(x-0.5)/0.1)+1] & \text{if } |x-0.5| < 0.1 \\ 0 & \text{otherwise} \end{cases} \tag{65}$$

on $0 < x < 1$ with $H(0) = 1$ and $g = 1$. The initial conditions were the stationary solution $u = 0$ and

$$\eta(x,0) = \begin{cases} H(0)+\epsilon & \text{if } 0.1 < x < 0.2 \\ H(0) & \text{otherwise.} \end{cases} \tag{66}$$

Theoretically, this disturbance splits into two waves, propagating left and right at the characteristic speeds $\pm\sqrt{gh}$. Many numerical methods have difficulty with the calculations involving such small perturbations of the water surface [6]. The solution at time $t = 0.7$ s for $\epsilon = 0.2$ m is shown in Fig. 20. A magnified view of the solution and comparison with the solution of LeVeque [6] is shown in Fig. 21. A computation for a smaller perturbation with $\epsilon = 0.01$ m was also carried out. A comparison of the present solution with that of LeVeque [6] at time $t = 0.7$ s is depicted in Fig. 22. It is clearly seen from these figures that the new scheme can provide a solution of accuracy comparable to that obtained with a high-resolution Godunov-type method based on balancing the source terms and flux gradients [6]. This suggests that the present scheme is able to handle small-perturbation problems occurring in shallow-water flows.

6.5. *A Hydraulic Jump in an Open Channel*

This test case illustrates the application of the SGM to treat bed friction terms, which are important in simulating a hydraulic jump, which occurs when the flow changes from a supercritical to a subcritical state in the direction of the flow. This is a stationary steady shock

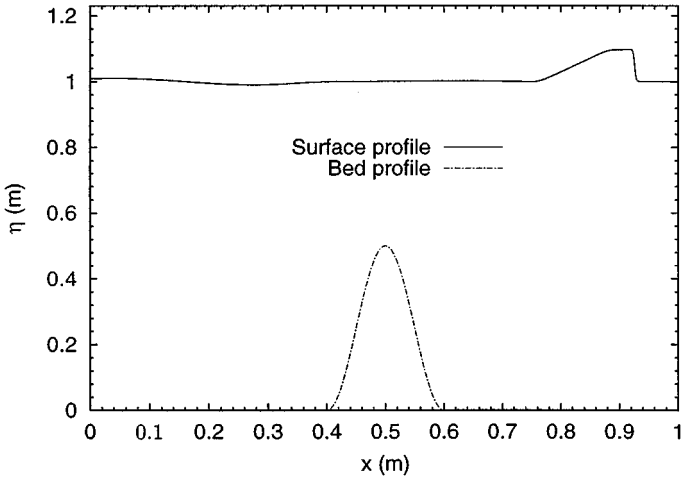

FIG. 20. Quasi-stationary case: Water surface elevation with small perturbation at $t = 0.7$ s.

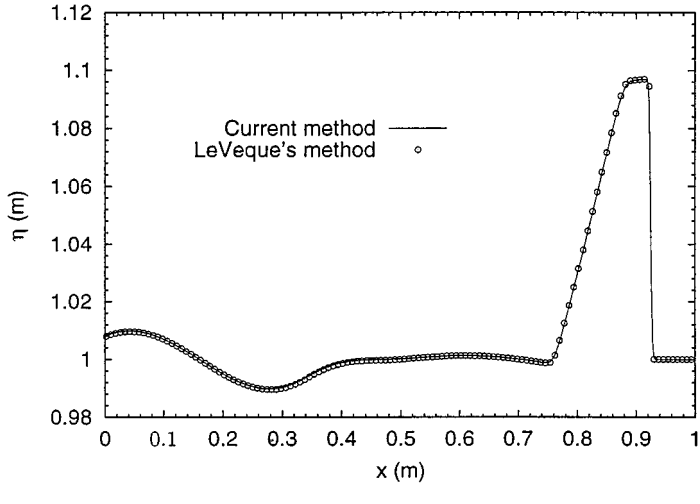

FIG. 21. Quasi-stationary case: Comparison of water surface elevations for $\epsilon = 0.2$ m.

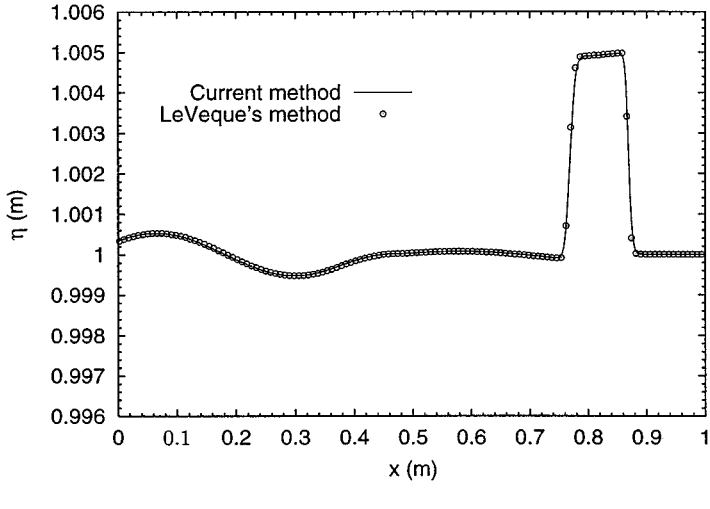

FIG. 22. Quasi-stationary case: Comparison of water surface elevations for $\epsilon = 0.01$ m.

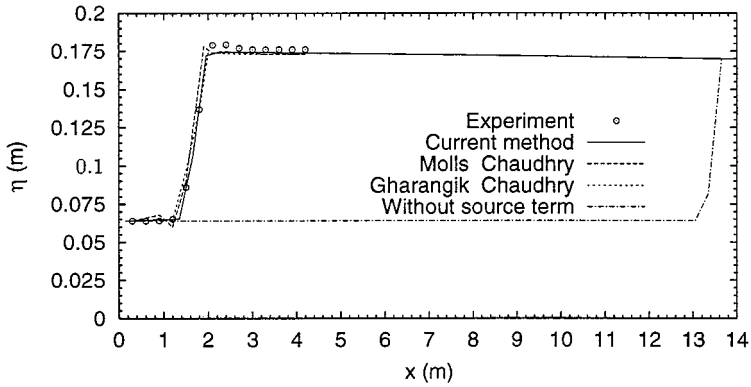

FIG. 23. Hydraulic jump: Comparison of water surface profiles ($Fr = 2.3$).

wave observed in open channels and natural rivers. According to the theory or open-channel hydraulics [16], if the flow conditions remain unchanged, the location of a hydraulic jump is largely determined in practice by the effect of bed roughness in the channel. This has also been demonstrated with a different numerical method [17]. Undoubtedly, the shallow-water equations without bed shear stress source terms are not generally applicable to simulating a hydraulic jump in a practical flow channel.

The channel was 14 m long and 0.46 m wide, the same dimensions as those used in the experiments [18]. There was no bed slope in the channel. The inflow Froude number was $Fr = 2.3$. The boundary conditions were: (1) inflow velocities $u = 1.92$ m/s and $v = 0$; the water depth $h = 0.064$ m; and (2) outflow depth $h = 0.168$ m. The boundary conditions and initial data were taken from the corresponding experimental data. A uniform mesh with 46×7 cells and mesh intervals $\Delta x = 0.3$ m and $\Delta y = 0.075$ m, together with bed friction coefficient $C_f = 0.00107$, were used in the computations. A steady-state solution was reached after 5865 iterations. Figure 23 shows the profile of the jump and a comparison with experimental data, numerical solutions obtained with different numerical methods [18, 19], and a computation made without the bed shear stress source terms, indicating that the location of the hydraulic jump is incorrectly predicted. The convergence history is plotted in Fig. 24.

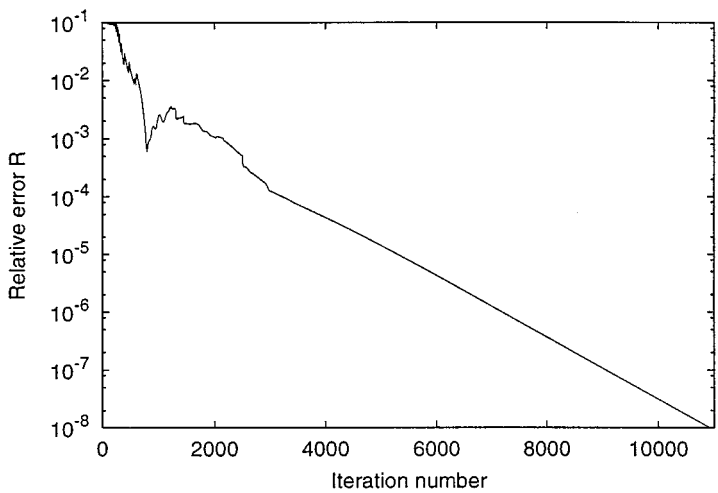

FIG. 24. Hydraulic jump: Convergence history ($Fr = 2.3$).

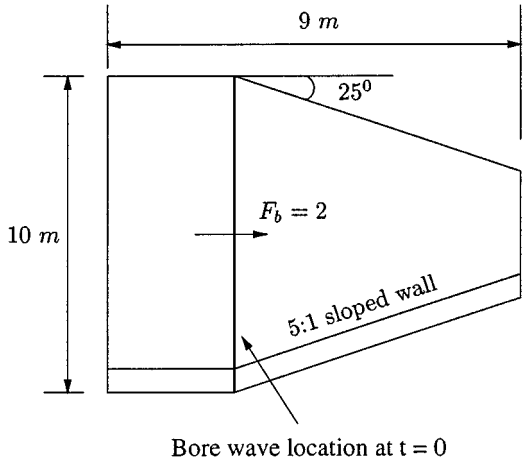

FIG. 25. Wave basin for bore reflection.

6.6. *Bore Reflection by a Sloped Wall*

The final test case demonstrates the capability of the present method for solving a 2D shallow-water flow problem. A bore reflection at a sea wall is of practical interest. Different types of the bore reflections have been investigated numerically by Mingham and Causon [2] for shallow-water flows. Here we consider a wave basin shown in Fig. 25 where the upper wall is vertical and the lower wall has a $5:1$ slope along its entire length. This will illustrate at the same time both oblique bore reflection at the vertical wall and the similar interaction occuring at the sloped wall. A bore wave travells from left to right along the basin and interacts with each side wall downstream. This problem is completely specified by the bore Froude number and the downstream state of the bore. The bore Froude number and the initial condition on the right state of the bore are

$$F_b = 2, \qquad \phi^{\mathrm{R}} = 9.81\ \mathrm{m}^2/\mathrm{s}^2, \qquad u^{\mathrm{R}} = v^{\mathrm{R}} = 0. \tag{67}$$

The initial condition on the left state of the bore can be determined from the shock conditions as

$$\frac{\phi^{\mathrm{L}}}{\phi^{\mathrm{R}}} = \frac{\sqrt{1+8F_b^2}-1}{2}, \qquad u^{\mathrm{L}} = F_b\left(1-\frac{\phi^{\mathrm{R}}}{\phi^{\mathrm{L}}}\right)\sqrt{\phi^{\mathrm{R}}}. \tag{68}$$

Theoretical analysis indicates that a single Mach reflection occurs under these conditions.

The SGM is incorporated on a body-fitted cut cell mesh which can efficiently treat irregular boundaries while retaining the simplicity of a Cartesian grid implementation. A detailed description of the cut cell method is given by Causon *et al*. [4]. One-hundred and twenty cells in flow direction and 108 cells in the transverse direction were used. The results at $t = 8$ s are sufficient to illustrate the flow physics. Figures 26 and 27 show the computed water surface looking toward the vertical and sloping walls, respectively. At the upper vertical wall, a well-developed triple point is visible with the formation of a Mach stem normal to the wall. At the lower sloping wall, the reflection pattern is similar; however, the reflected wave is weaker and the foot of the Mach stem appears to be oriented slightly further forward on the wall due to the effect of wall slope. Contours of the water surface elevation are plotted in Fig. 28.

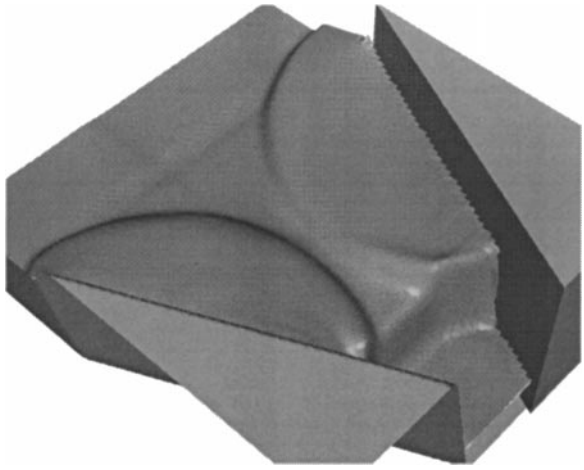

FIG. 26. Single Mach reflection: Water surface looking toward the upper (vertical) wall.

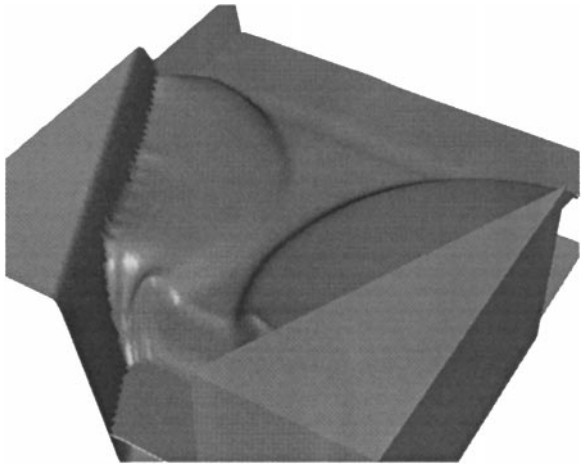

FIG. 27. Single Mach reflection: Water surface looking toward the lower (sloping) wall.

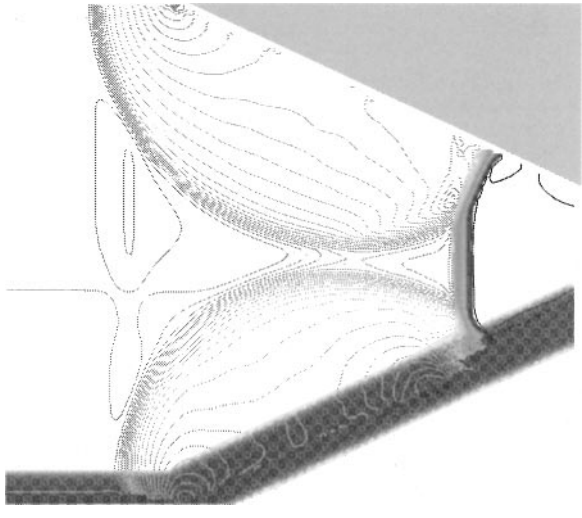

FIG. 28. Single Mach reflection: Line contours of water surface elevation.

7. CONCLUSIONS

An accurate data reconstruction procedure for use in a high-resolution Godunov-type finite volume method applied to the shallow-water equations with bed slope source terms has been presented. The scheme is as simple and efficient as a conventional piecewise linear reconstruction method and enables the source terms to be discretized with a centered discretization scheme. The proposed procedure can provide accurate values for the conservative variables at cell interfaces and fully retains the conservative property of the parent finite-volume scheme. Using the new method, the fluxes at cell interfaces can be accurately calculated with a Riemann solver with few errors being introduced by the inclusion of the bed slope terms. The scheme has been successfully applied to a selection of steady and unsteady problems. These benchmark tests have shown that the scheme provides accurate solutions in excellent agreement with the corresponding analytical solutions. The results also demonstrate that the scheme is accurate, simple, efficient, and robust. The SGM together with an appropriate Godunov-type finite-volume method is suitable for solving practical shallow-water flow problems involving bed slope source terms.

ACKNOWLEDGMENTS

Funding from the Manchester Metropolitan University, U.K., is gratefully acknowledged.

REFERENCES

1. F. Alcrudo and P. Garcia-Navarro, A high-resolution Godunov-type scheme in finite volumes for the 2d shallow-water equations, *Int. J. Numer. Methods Fluids* **16**, 489 (1993).
2. C. G. Mingham and D. M. Causon, High-resolution finite-volume method for shallow water flows, *J. Hydraul.-Eng. ASCE* **124**, 605 (1998).
3. K. Hu, C. G. Mingham, and D. M. Causon, A bore-capturing finite volume method for open-channel flows, *Int. J. Numer. Methods Fluids* **28**, 1241 (1998).
4. D. M. Causon, D. M. Ingram, C. G. Mingham, G. Yang, and R. V. Pearson, Calculation of shallow water flows using a Cartesian cut cell approach. *Adv. Water Resour*. **23**, 545 (2000).
5. E. F. Toro, *Riemann Solvers and Numerical Methods for Fluid Dynamics* (Springer-Verlag, Berlin/Heidelberg, 1997).
6. R. J. LeVeque, Balancing source terms and flux gradients in high-resolution Godunov methods: The quasi-steady wave-propagation algorithm, *J. Comput. Phys.* **146**, 346 (1998).
7. A. Bermudez and M. E. Vázquez, Upwind methods for hyperbolic conservation laws with source terms, *Comput. Fluids* **23**, 1049 (1994).
8. M. E. Vázquez-Cendón, Improved treatment of source terms in upwind schemes for shallow water equations in channels with irregular geometry, *J. Comput. Phys.* **148**, 497 (1999).
9. R. J. LeVeque, *Numerical Methods for Conservation Laws* (Birkhäuser-Verlag, Basel, 1990).
10. B. van Leer, On the relation between the upwind-differencing schemes of Godunov, Enguist–Osher and Roe, *SIAM J. Sci. Stat. Comput.* **5**, 1 (1985).
11. A. Harten, P. Lax, and B. van Leer, On upstream differencing and Godunov-type schemes for hyperbolic conservation laws, *SIAM Rev.* **25**, 35 (1983).
12. E. F. Toro, Riemann problems and the WAF method for solving two-dimensional shallow water equations, *Philos. Trans. R. Soc. London Ser. A* **338**, 43 (1992).
13. L. Fraccarollo and E. F. Toro, Experimental and numerical assessment of the shallow water model for two-dimensional dam-break type problems, *J. Hydraul. Res.* **33**, 843 (1995).
14. A. Bermudez, A. Dervieux, J. Desideri, and M. E. Vázquez, Upwind schemes for the two-dimensional shallow water equations with variable depth using unstructured meshes, *Comput. Methods Appl. Mech. Eng*. **155**, 49 (1998).

15. N. Goutal and F. Maurel, eds., *Proceedings of the 2nd Workshop on Dam-Break Wave Simulation*, HE-43/97/016/B (Département Laboratoire National d'Hydraulique, Groupe Hydraulique Fluviale Electricité de France, France, 1997).
16. V. T. Chow, *Open-Channel Hydraulics* (McGraw-Hill, New York, 1959).
17. J. G. Zhou and P. K. Stansby, 2D shallow water model for hydraulic jump, *Int. J. Numer. Methods Fluids* **29**, 375 (1999).
18. A. M. Gharangik and M. H. Chaudhry, Numerical simulation of hydraulic jump, *J. Hydraul. Eng. ASCE* **117**, 1195 (1991).
19. T. Molls and M. H. Chaudhry, Depth-averaged open-channel flow model, *J. Hydraul. Eng. ASCE* **121**, 453 (1995).